# **Upgrade and application of the gas puff imaging system in EAST**

S.C. Liu<sup>a, \*</sup>, L. Liao<sup>a, b</sup>, L.J. Zhong<sup>c</sup>, W. Wei<sup>c</sup>, L.T. Li<sup>a, d</sup>, W.Y. Wei<sup>a, b</sup>, N. Yan<sup>a</sup>, Y.L. Xing<sup>a</sup>, G.S. Xu<sup>a</sup>, L.M. Shao<sup>a</sup>, R. Chen<sup>a</sup>, G.H. Hu<sup>a</sup>, J.B. Liu<sup>a</sup>, Y. Liang<sup>a, e</sup>, X. Han<sup>a</sup>, J. Cai<sup>a</sup>, N. Zhao<sup>f</sup>, X.J. Liu<sup>a</sup>, T.F. Ming<sup>a</sup>, Q. Zang<sup>a</sup>, L. Wang<sup>a</sup>, L. Zeng<sup>a</sup>, G.Q. Li<sup>a</sup>, X.Z. Gong<sup>a</sup>, X. Gao<sup>a</sup> and EAST Team

- <sup>a</sup> Institute of Plasma Physics, Chinese Academy of Sciences, 230031, Hefei, Peoples Republic of China
- <sup>b</sup> University of Science and Technology of China, 230026, Hefei, Peoples Republic of China
- <sup>c</sup> Institute of Optics and Fine Mechanics, Chinese Academy of Sciences, 230031, Hefei, Peoples Republic of China
- <sup>d</sup> Anhui University, 230039, Hefei, People's Republic of China
- <sup>e</sup> Forschungszentrum Jülich GmbH, Institut für Energie und Klimaforschung Plasmaphysik, Partner of the Trilateral Euregio Cluster (TEC), 52425, Jülich, Germany
- f School of Science, Southwest University of Science and Technology, 621010, Mianyang, China E-mail: shaocheng.liu@ipp.ac.cn

#### Abstract

The gas puff imaging (GPI) system on EAST has been developed in 2012 and upgraded in 2021. A new relay optical system, consisting of a front reflecting prism, a series of lens and a filter, is developed for the GPI diagnostic. At the end of the relay optical system, the rays are focused to a thin image surface, which is captured by the sensor of a high-speed camera. In contrast with the previous optical system of GPI in which a coherent glass fiber bundle is used to transmit image from the end of telescope inside the vacuum vessel to the outside, the new relay optical system has much lower light loss, i.e., the emission intensity on the image plane is much higher in the new optical system. In consequence, the temporal resolution of GPI diagnostic on EAST can be raised significantly. The analysis of the optical design denotes that the imaging quality is high enough to ensure a spatial resolution of 2 mm on the objective plane. In the spring experimental campaign of 2021, the upgraded GPI system has been commissioned in EAST. Clear poloidal and radial propagations of the edge fluctuations are measured directly by GPI with a high sampling rate of 530 kHz. The poloidal and radial velocities of the edge fluctuations are derived by the time-delay cross-correlation method, with radial velocity propagating outward, and poloidal velocity propagating in the ion-diamagnetic drift direction in the SOL and in the electron-diamagnetic drift direction inside the LCFS.

Keywords: gas puff imaging, GPI, turbulence, scrape-off layer, EAST, tokamak, plasma

## 1. Introduction

Understanding turbulence transport is one of the most important issues in tokamaks and stellarators [1, 2]. Since plasma turbulence is driven by free energy sources for microinstabilities, the edge turbulence could play an important role in the energy and particle transports due to the radial gradient of plasma temperature and density in the boundary region [1]. In the low-confinement mode (L-mode), blobs are generated in the edge plasma and ejected into the scrape-off layer (SOL), carrying heat and particle across the magnetic field, and leading to intermittent transport [3-5]. The interaction between edge turbulence and zonal flow via Reynolds stress plays a key role in the low-to-high (L-H) confinement mode transition [6-8]. In EAST, an edge coherent mode exhibiting

the nature of dissipative trapped electron mode contributes to continuous radial heat and particle outflow and greatly facilitates the long pulse H-mode sustainment [9]. When the edge localized modes (ELMs) are mitigated or suppressed by the resonant magnetic perturbations (RMPs), turbulence is found to increase significantly over a wide radial region and affect the local transport in DIII-D [10], and a broadband turbulence which drives outward heat and particle fluxes is enhanced greatly in EAST [11]. Some diagnostics have been developed to measure the edge turbulence in magnetically confined plasmas, such as Langmuir probe [12], beam emission spectroscopy [13], phase contrast imaging [14], reflectometry [15], electron cyclotron emission imaging [16].

Gas puff imaging (GPI) is a direct method to measure the two-dimensional (2D) structure of edge turbulence [17].

Usually neutral gas (deuterium or helium) is puffed into the plasma edge and a gas cloud is formed on the objective plane, then a visible light emission from the gas cloud is imaged to a high speed camera through an optical system [18]. According to some modelling works [19-21], the neutral atom line emission intensity measured by GPI can be expressed as

$$I = n_0 f(n_e, T_e), \tag{1}$$

where  $n_0$  is the local neutral atom density,  $n_e$  and  $T_e$  are the local electron density and temperature, respectively. The function f is the ratio of the density at the upper level of the radiative transition to the ground state density times the radiative decay rate for the transition. For the helium gas puff, the function f can be expressed as

$$f \propto n_e^{\alpha_n} T_e^{\alpha_T} \,, \tag{2}$$

with the exponent  $\alpha_n$  close to 1 in relatively low density case and less than 1 in higher density case, and  $\alpha_T$  decreasing monotonically between  $T_e = 1{\text -}100 \text{ eV}$  [18, 22, 23]. Thus, the fluctuations of the GPI light emission depend on the electron density and temperature fluctuations.

The GPI diagnostic has been applied to the edge turbulence measurement in many fusion devices, such as NSTX [24], Alcator C-Mod [25], ASDEX-U [26], TEXTOR [27], Heliotron J [28], HL-2A [29], etc. A dual GPI diagnostic system with up-down symmetrical views has been developed in the EAST tokamak in 2012 [30]. The same as most of the GPI systems mentioned above, the previous GPI system in EAST consisted of a gas manifold, a telescope, a coherent glass fiber bundle and a high speed camera. In the front of the telescope, a mirror is used to deflect the light from gas cloud into the lens capsule; at the end of the telescope, the image is collected and transmitted to the outside of vacuum chamber by a 400×400 pixel coherent glass fiber bundle. Between the fiber bundle and camera, a pair of lenses (focal length: 75 mm and 25 mm) is adopted to de-magnify the image onto a small region of the camera sensor. The application of fiber bundle makes it flexible to install and calibrate the optical system in the torus hall, which is extremely convenient when the space is limited at the port flange. Because the fiber bundle has much larger numerical aperture than the lens at the end of fiber, there is considerable light loss at the interface of fiber bundle and this lens. Furthermore, the diameter of the 75 mm lens that is connected to the fiber is about twice larger than the 25 mm lens that is connected to the camera, consequently only a small part of light could reach the camera sensor, which leads to a weak emission intensity on the image plane. The EAST GPI system has been shifted from D port to O and P ports in 2014, and this diagnostic has been suffering a weak image intensity since then. It is critical to increase the light intensity and improve the temporal resolution of GPI in EAST. The rest of this paper is organized as follows. The upgrade of GPI is given in section 2. The commissioning experimental results are presented in section 3. Section 4 is a summary.

# 2. Upgrade of GPI in EAST

## 2.1 Layout of GPI system in EAST

EAST is a superconducting tokamak with a major radius 1.9 m, a minor radius 0.45 m [31]. Integrated optimization of the EAST diagnostic system has been executed in 2020 to improve the corresponding performance in long-pulse discharge. In order to solve the problem of GPI in EAST as mentioned in section 1, a new optical system has been developed since 2020 and the installation on site was finished in the spring of 2021.

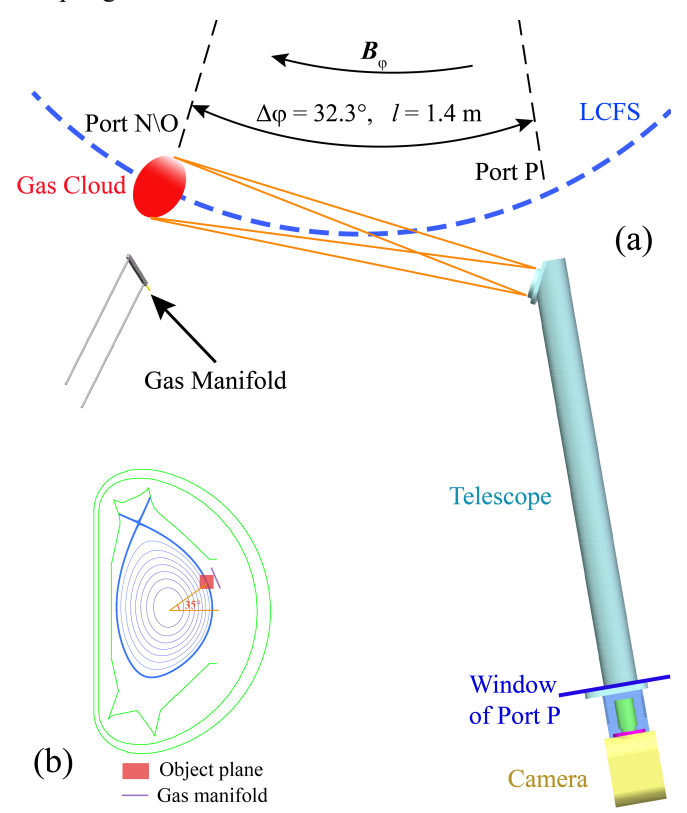


Fig. 1. (a) The toroidal layout of the GPI on EAST viewed from top; (b) poloidal layout viewed in anti-clockwise direction.

The upgraded GPI is illustrated in Fig. 1. The optical system is located at the outer midplane of port P, and the gas manifold is in the middle of ports N and O. Helium is puffed into the edge plasma by the gas manifold with 22 holes of 0.5 mm diameter spaced by 10 mm apart from 210 mm in a linear array. For typical magnetic configurations in EAST, the center of the 130×130 mm objective plane is on the last closed flux surface (LCFS), and the objective plane covers 65 mm in the SOL and 65 mm inside the LCFS, as shown in Fig. 1 (b). Note that the objective plane is about 27.6 cm above the outer midplane, with a poloidal angle of 35° between the horizontal plane and the minor radius of objective plane center. The

toroidal angle between the gas cloud illustrated by the red ellipse in Fig. 1 (a) and the prism center of the optical system is 32.3°, and the corresponding optical length is 1.4 m. The

sightline of the optical system is along the local magnetic field at the gas cloud center when the toroidal field is in clockwise direction viewed from top.

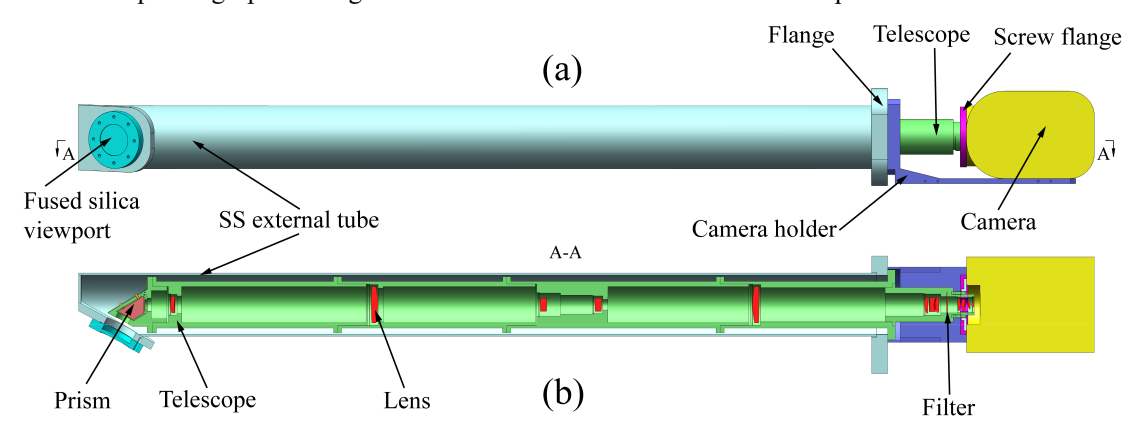


Fig. 2. (a) Sketch of the mechanical structure of the GPI optical system; (b) the cut-away view of A-A with the cut face shown in (a).

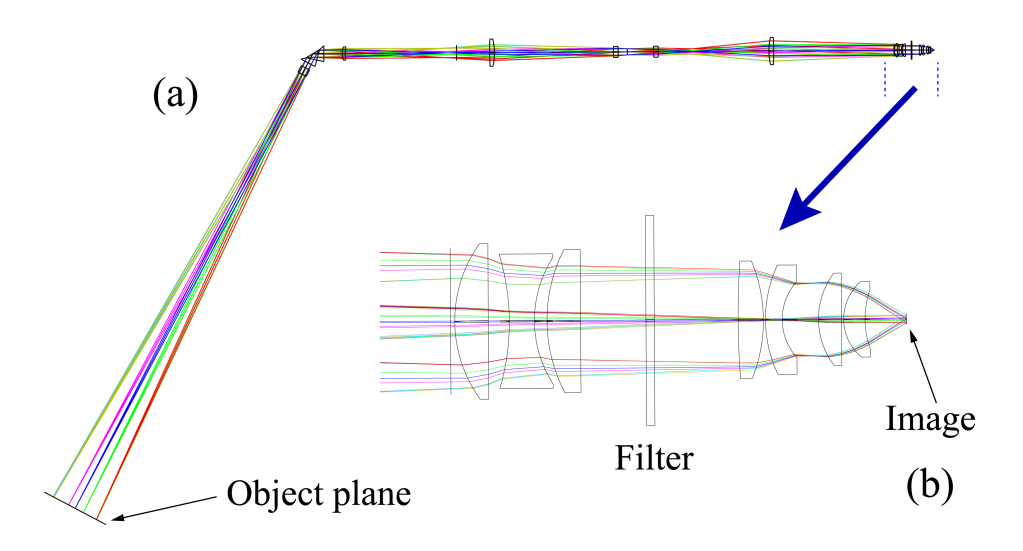


Fig. 3. (a) Optical design of the GPI system on EAST; (b) zoom in optical system of the filter and image.

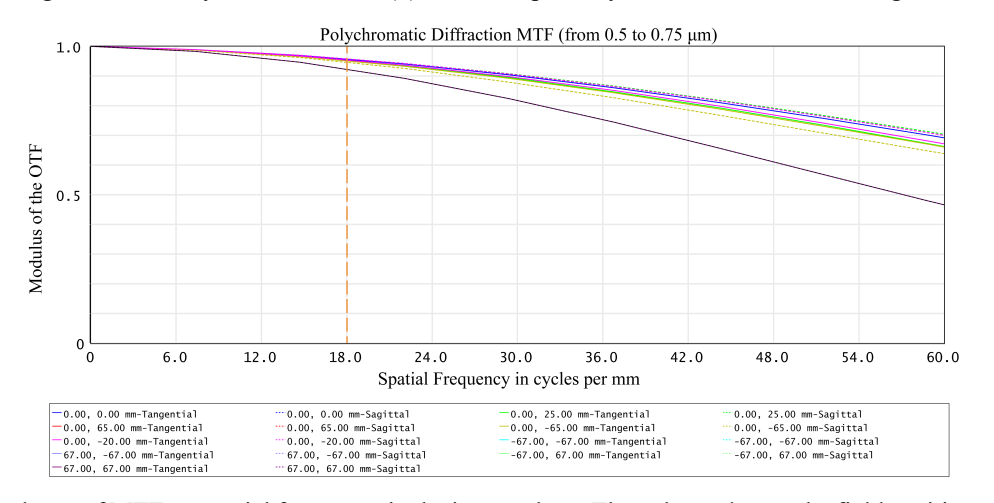


Fig. 4. The dependence of MTF on spatial frequency in the image plane. The colours denote the field position on the objective plane. The solid line means the data computed in the tangential plane, while the dashed line means the data computed in the sagittal plane.

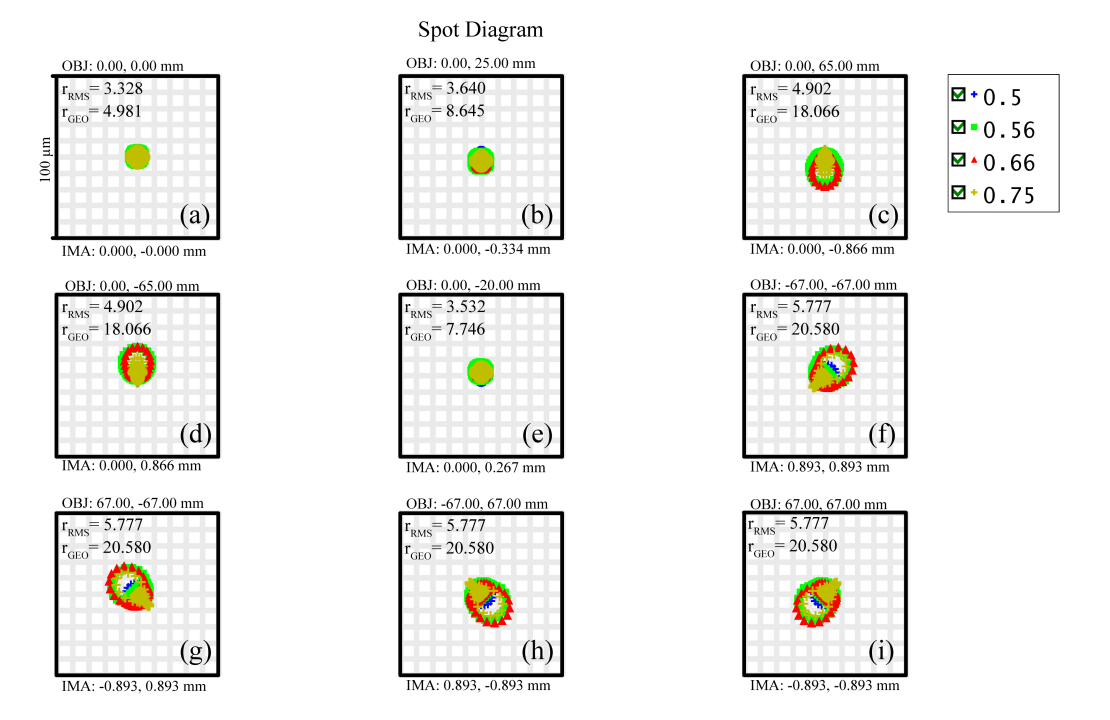


Fig. 5. Spot diagram of 9 points on the objective plane for four wavelengths. In each panel, the point position on objective plane is at the top; the corresponding position on the image plane is at the bottom; the RMS and GEO spot radiuses are annotated inside each panel.

# 2.2 Mechanical structure of optical system

The mechanical structure of the optical system is composed by an inner cylinder and an outer cylinder, as illustrated in Fig. 2. The main body of the outer cylinder is a long pipe, whose front surface is an oblique plane connected to a fused silica viewport through a CF flange. The end of the cylinder pipe is welded with a large flange, the front surface of which faces the window of port P, and a FKM ring is used to seal the vacuum. After assembly and installation of the outer cylinder, the vacuum is isolated by both the front fused silica view port and the back flange, consequently it is atmosphere inside the pipe. As shown in Fig. 2, the 'L' shape camera holder is fixed at the back flange of the outer cylinder through bolts. The high-speed camera is also fixed on the camera holder by bolts, and the camera position can by adjusted fine to align the image on the central pixels of camara sensor by the bolts connecting the camera holder and the outer cylinder. The front part of the out cylinder is protected by a shutter which is driven by an electric motor and moves linearly. All the optical elements are integrated in the inner cylinder. Aiming to fix and adjust the prism and lenses conveniently, the inner cylinder is divided into six segments, as illustrated in Fig. 2 (b). The first segment in the front of the inner cylinder is a prism and its holder. Note that the titled angle of the prism can be changed by the orange Teflon jackscrews in Fig. 2 (b). All the lenses are installed in the following five segments. Two adjacent segments are connected by bolts. The filter is fixed in a slot and can be replaced in an experimental campaign. This separated structure of inner and outer cylinders makes it possible to maintain the optical systems without removing the outer cylinder and shutter, i.e., having no impact on the vacuum chamber.

# 2.3 Design of optical system

The optical design of the GPI system on EAST is shown in Fig. 3. From the front of optical system to the back, there is a silica viewport, a prism, 12 lenses and a filter. The light from the 13×13 cm objective plane firstly passes the viewport, and it is deflected by the prism and transmitted by the lenses in the long cylinder. In the last segment of the inner cylinder in Fig. 2 (b), the rays are parallel to the primary optical axis, as illustrated in Fig. 3 (b). A single-band bandpass filter located in the parallel ray region has a center wavelength of 587 nm and a bandwidth of 11 nm with transmission rate over 93%. At the end of the optical system, the rays are focused to the image plane and collected by the sensor (1.972×1.972 mm, corresponding to 64×64 pixels) of a high-speed camera. Note that all the optical elements, including viewport, prism, and lenses, are coated to raise the light transmission rate over 99% in the 500-750 nm wavelength band. In consequence, the light transmission rate of GPI optical system can be up to 70%.

The spatial resolution and the image quality can be estimated from the optical transfer function (OTF) and spot diagram. The modulation transfer function (MTF) from 500 to 750 nm is shown in Fig. 4, with the colours denoting the field position on the objective plane. Phantom V1610 camera is adopted in the EAST GPI system. The size of each pixel is  $28 \times 28 \, \mu m$ , and the corresponding spatial frequency is  $35.7 \, m$ 

mm<sup>-1</sup>. According to the Nyquist-Shannon sampling theorem [32], the sampling rate should be larger than twice of the maximum frequency contained in the signal, therefore the maximum spatial resolution on the camera sensor is about 18 mm<sup>-1</sup>, which is labelled by the yellow dashed line in Fig. 4. The MTF is larger than 0.9 at spatial frequency 18 mm<sup>-1</sup> which means excellent imaging quality, and the MTF is larger than 0.5 when spatial frequency smaller than 55 mm<sup>-1</sup> for all the positions in the objective plane. In consequence, the spatial resolution on the objective plane is determined by the number of sensor pixels on the image plane, i.e.,  $130 \text{ mm/}64 \approx 2 \text{ mm}$ . The spot diagram of 9 points on the objective plane for 4 wavelengths are presented in Fig. 5. In each panel, the point positions on the objective plane and image plane are given at the top and bottom, respectively. The root-mean-square (RMS) spot radius size and the GEO spot radius size are annotated inside each panel, with GEO radius denoting the largest distance from the center of spot cluster to the ray. As illustrated in Fig. 5, the maximum RMS spot radius is 5.8 µm that is much smaller than the pixel size of 28 µm, signifying that most of the energy is concentrated in a circle region with very small radius compared with the pixel size. The GEO spot radius is about 5–8.6 µm in the central region of the objective plane, and about 20.6 µm at the boundary, which is also smaller than the pixel size. The four wavelengths from 500 nm to 750 nm reveal similar ray distribution in the spot diagram, indicating good focusing characteristic.

In summary, the GPI optical system collects the light emission from the  $130 \times 130$  mm gas cloud and forms the image on the sensor with a size of  $1.972 \times 1.972$  mm, with a magnification factor about 0.0135. The light transmission rate of GPI optical system can be up to 70% with an entrance pupil diameter of 19 mm. The spatial resolution is about 2 mm on the objective plane, and the spot size is much smaller than the pixel size on the image plane.

## 3. Experimental results

The upgraded GPI diagnostic has been commissioned in the spring of 2021. The high speed camera is operated with a speed of 531645 frames/s and a resolution of 128×64 pixels (3.584×1.792 mm) that covers the image of objective plane (1.972×1.972 mm). The plasma parameters of an L-mode discharge 103881 are as follows: toroidal magnetic field  $B_t$  = 2.6 T in clockwise direction viewed from top, plasma current  $I_p = 500$  kA, safety factor at 95% normalized poloidal flux surface  $q_{95} = 5.3, 4.6$  GHz lower hybrid wave (LHW) heating power 0.6 MW, and line integrated electron density  $n_{el}$  = 2.7×10<sup>19</sup> m<sup>-2</sup>, as illustrated in Fig. 6 (a). The GPI diagnostic is triggered at 4.5 s, as displayed by the red pulse in Fig. 6 (c). At the same time, about 180 Pa.L helium gas is puffed into the plasma edge by switching on a piezoelectric gas leak valve for 30 ms. Note that the gas puff system is the same as that used in 2012 [30]. The GPI averaged emission intensity is presented by the black line in Fig. 6 (c), and it increases significantly from 75 to 490 at 4.55 s, i.e., 50 ms after the opening of valve, then it decreases slowly to 160 at 4.9 s. The signal-to-noise ratio during this 350 ms period is from 6.5 to 2. As illustrated in Fig. 6 (a), the impact of helium gas puff on the line integrated density  $n_{el}$  and the plasma stored energy can be ignored. Note that the increase of  $n_{el}$  at 4.55 s is caused by the supersonic molecular beam injection (SMBI), as illustrated in Fig. 6 (b).

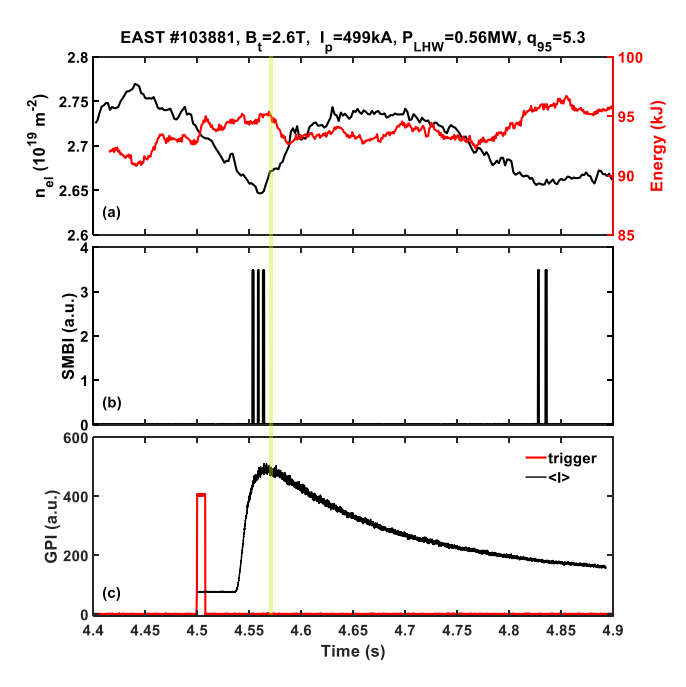


Fig. 6. Temporal evolution of plasma parameters of discharge 103881. (a) Plasma line integrated electron density and plasma stored energy; (b) SMBI signal; (c) GPI trigger pulse and the averaged emission intensity. The yellow vertical shadow denotes the time slice for Fig. 7.

## 3.1 Temporal evolution of GPI fluctuations

The temporal evolution of edge fluctuations around t =4.5710 s as labelled by the yellow shadow region in Fig. 6 is measured by GPI and illustrated in Fig. 7. In the processes of data analysis, firstly remove the background emission intensity from the raw data, secondly subtract the averaged emission intensity in the interested time period (from 4.571013 s to 4.571098 s for Fig. 7), finally obtain the GPI image of fluctuations. Aiming to characterize the evolution of edge turbulence with a complete view, the GPI images are shown every three frames with a time interval of 5.6 µs. In each panel, the LCFS is given in the purple dashed line, and the limiter is illustrated in the green dashed line. As shown in Fig. 7 (a), there are three pieces of positive GPI fluctuations located inside the LCFS, and they are distributed along the local magnetic surface, moving upward (electron-diamagnetic drift direction) continuously along poloidal direction. For example, the bottom piece of positive fluctuations gets stronger and moves poloidally from Z = 0.21 m to 0.28 m, as

illustrated in Fig. 7 (a-p). Outside the LCFS, there are several pieces of positive fluctuations which are also distributed to match the tilted angle of local magnetic surface, as shown in Fig. 7 (a). The GPI fluctuations outside the LCFS propagate downward poloidally (ion-diamagnetic drift direction) and outward radially, as presented in the time sequence of GPI images from Fig. 7 (a) to (p). The positive GPI fluctuations crossing the LCFS are observed at  $Z=0.3\,\mathrm{m}$  from Fig. 7 (g) to (n). Similar radial propagations of fluctuations crossing LCFS are also found at  $Z=0.32\,\mathrm{m}$  and 0.23 m in Fig. 7. Note that the emission intensity of GPI gas cloud is almost keeping the same in this short time, i.e., the GPI fluctuations signify the variations of edge turbulence.

# 3.2 Propagation velocity

The propagation velocity of GPI fluctuations is calculated by the time-delay cross-correlation method [30, 33, 34]. The poloidal and radial velocity measured by GPI is presented in Fig. 8 for discharge 103881. The vertical axis dr is the distance from LCFS at t = 4.55 s along the minor radius. It

should be pointed out that the position of LCFS from EFIT equilibrium has an uncertainty about 1 cm. The poloidal velocity is directed upward (electron-diamagnetic drift direction) inside the LCFS and downward (ion-diamagnetic drift direction) outside the LCFS, as shown in Fig. 8 (b). From t = 4.55 s to 4.7 s, the separatrix between the positive and negative  $V_{\theta}$  is stable, though the separatrix moves outward slightly within t = 4.58-4.63 s. From the far SOL to the LCFS, the amplitude of the negative  $V_{\theta}$  increases to 1–2 km/s gradually but decreases quickly to zero near the LCFS; from the LCFS to dr = -2 cm, the positive  $V_{\theta}$  increases to 2-3 km/s. As illustrated in Fig. 8 (a), the radial velocity is mainly directed outward. In the SOL,  $V_r$  peaks at dr = 1 cm with a speed of 0.2–0.5 km/s; inside the LCFS,  $V_r$  peaks at dr = -1.2 cm with a speed of 0.2-1 km/s; while V<sub>r</sub> is below 0.2 km/s from dr = -0.5 cm to 0.5 cm. In addition, the radial velocity reveals strong intermittent characteristics, indicating the existence of intermittent transport.

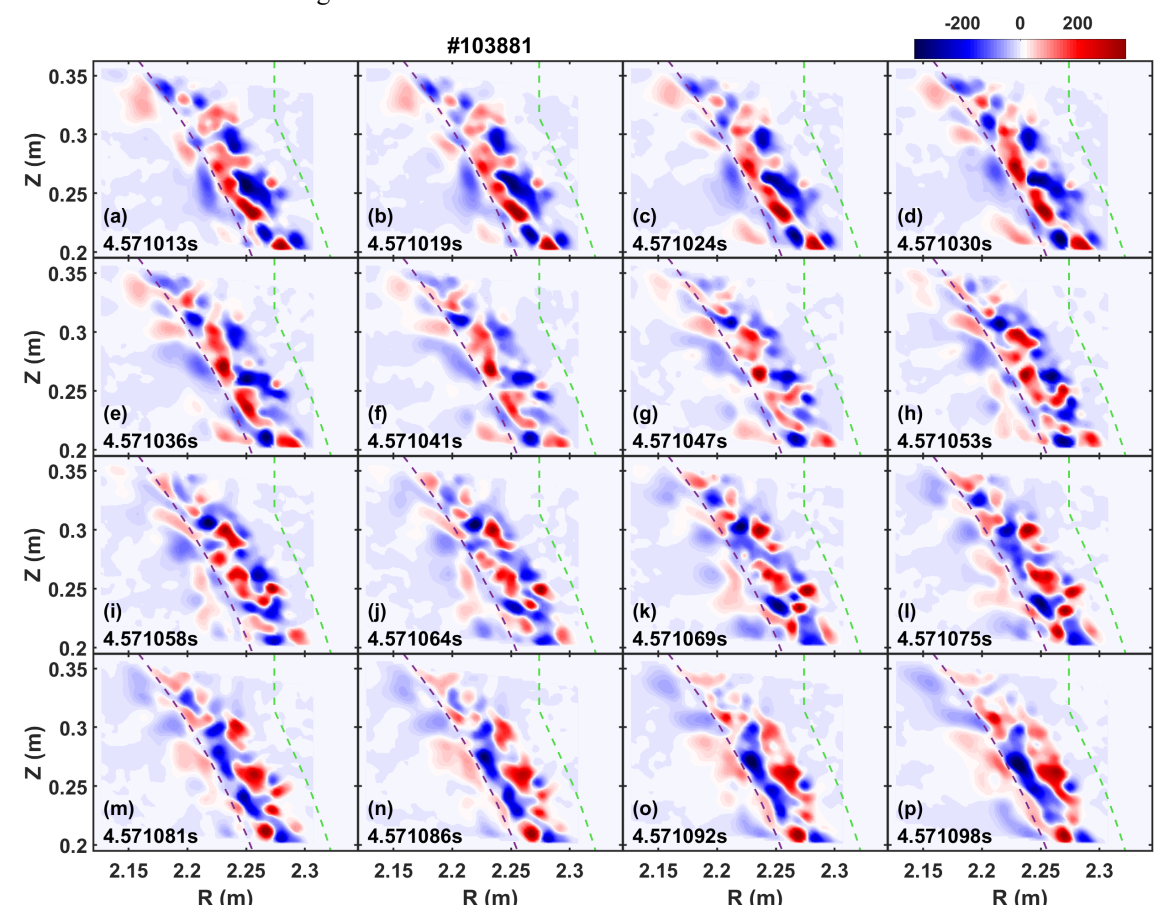


Fig. 7. (a-p) GPI images are shown every three frames, with the horizontal axis as the major radius and the vertical axis in vertical direction. The time slice is annotated in each panel. The LCFS is given in the purple dashed line, and the limiter is illustrated in the green dashed line.

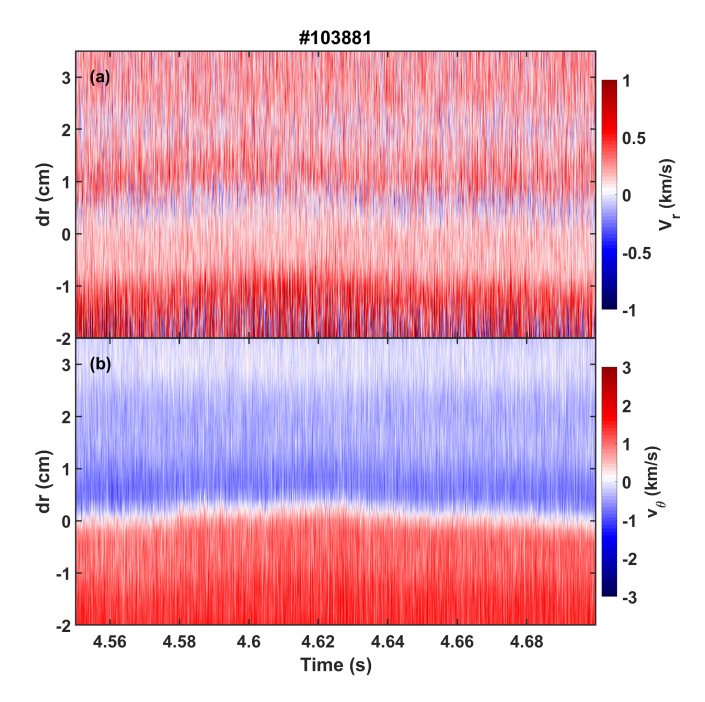


Fig. 8. Radial velocity (a) and poloidal velocity (b) measured by GPI for discharge 103881. The vertical axis is the distance from LCFS along the minor radius. Positive  $V_r$  is directed outward, and positive  $V_{\theta}$  is directed upward (electron-diamagnetic drift direction).

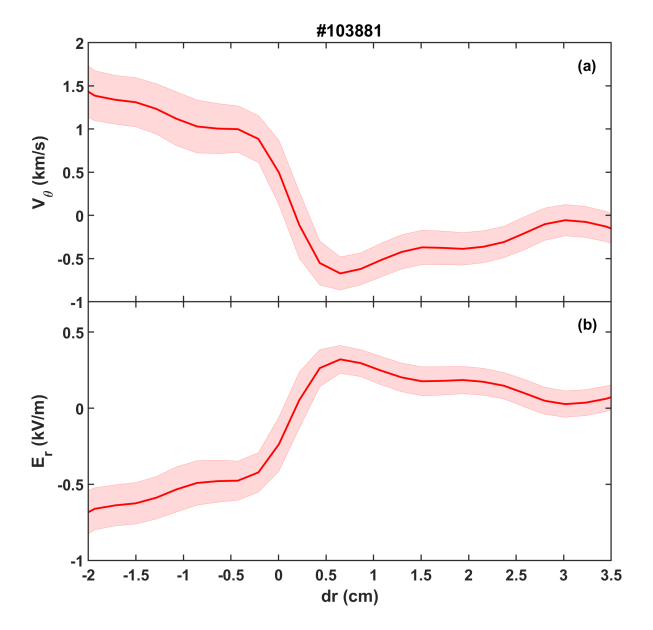


Fig. 9 The radial profiles of poloidal velocity (a) and radial electric field (b). The shaded region denotes the standard deviation of the measurement. Positive  $V_{\theta}$  is directed upward (electron-diamagnetic drift direction). Positive  $E_r$  is directed outward radially.

The time averaged poloidal velocity between t = 4.55-4.7 s is presented in Fig. 9 (a), and it is negative in the SOL and positive inside the LCFS, with direction changing sharply around the LCFS. The radial electric field is derived from the

poloidal velocity by  $E_r = V_\theta/B_t$ , as illustrated in Fig. 9 (c). In the SOL,  $E_r$  is directed outward and peaks in the near SOL with a value about 0.3 kV/m, then decreases quickly and changes to inward direction around the LCFS. Inside the LCFS, the amplitude of  $E_r$  increases gradually and reaches  $E_r = -0.65$  kV/m at dr = -2 cm. The poloidal velocity and radial electric field are similar with that measured by reciprocating probe in EAST [35].

## 4. Summary

The EAST GPI diagnostic has been upgraded by developing a new relay optical system in 2020 and operated successfully in the spring experimental campaign of 2021. The new optical system, consisting of a silica viewport, a prism, 12 lenses and a filter, collects the light emission from the gas cloud and focuses the rays to the image plane of camera sensor. All the optical elements are coated to raise the light transmission over 99% in the 500-750 nm wavelength band, and the light transmission rate of the GPI optical system can be up to 70%. The GPI optical system has high spatial resolution and image quality, as estimated by the modulation transfer function and spot diagram. The high speed camera is operated with a speed of 531645 frames/s and a resolution of 128×64 pixels. The spatial resolution of the GPI system is 2 mm in the objective plane. The mechanical structure of the optical system is composed by an outer cylinder and an inner cylinder that contains a prism and lenses, which is a big convenience for maintaining the optical system. In contrast with the previous GPI optical system in EAST in which a coherent glass fiber bundle is used to transmit image from the end of a telescope to the high speed camera, the new relay optical system has much lower light loss, consequently the image intensity and the GPI temporal resolution can be raised significantly, as demonstrated by the commissioning experiment of GPI. The signal-to-noise ratio of GPI emission intensity can be up to 6.5 that is large enough to analyze the edge turbulence structure. Meanwhile, the helium gas puff of GPI diagnostic has very weak impact on the line integrated electron density and plasma stored energy, which is beneficial to the understanding of GPI data. The plasma fluctuations measured by GPI diagnostic move poloidally in the iondiamagnetic drift direction in the SOL and in the electrondiamagnetic drift direction inside the LCFS. Clear outward propagation of fluctuations is also observed in the time sequence of GPI images. The poloidal velocity derived by the time-delay cross-correlation method reveals clear radial structure, i.e., it is negative in the SOL and positive inside the LCFS, which is consistent with the observation from the time sequence of GPI images. The radial velocity is directed outward in the whole radial range measured by GPI. The radial electric field derived from the poloidal velocity is consistent with that measured by reciprocating probe in EAST. The successful upgrade of GPI diagnostic will contribute to the study of edge turbulence structure and evolution in EAST.

# Acknowledgement

The authors greatly acknowledge S.J. Zweben for the valuable discussion on the development of GPI diagnostic in EAST tokamak. This work was supported by the National MCF Energy R&D Program (Nos. 2019YFE03030000 and 2017YFE0301205), the National Natural Science Foundation of China under grant contract No. 11875294k, 12175277 and 12005144, the Science Foundation of Institute of Plasma Physics, Chinese Academy of Sciences, No. DSJJ-2021-01, the Collaborative Innovation Program of Hefei Science Center, CAS, No. 2021HSC-CIP019, and the Users with Excellence Program of Hefei Science Center, CAS under grant Nos. 2021HSC-UE014.

## References

- [1] Doyle E. J. et al Chapter 2: Plasma confinement and transport, Nucl. Fusion 47 (2007) S18
- [2] Wakatani M. et al Chapter 2: Plasma confinement and transport, Nucl. Fusion 39 (1999) 2175
- [3] D'Ippolito D. A. *et al* Convective transport by intermittent blob-filaments: Comparison of theory and experiment, Phys. Plasmas 18 (2011) 060501
- [4] Zweben S. J. *et al* Blob structure and motion in the edge and SOL of NSTX, Plasma Phys. Control. Fusion. 58 (2016) 044007
- [5] Nielsen A. H. *et al* Numerical simulations of blobs with ion dynamics, Plasma Phys. Control. Fusion. 59 (2017) 025012
- [6] Diamond P. H. *et al* Zonal flows in plasma a review, Plasma Phys. Control. Fusion. 47 (2005) R35
- [7] Xu G. S. *et al* First Evidence of the Role of Zonal Flows for the L-H Transition at Marginal Input Power in the EAST Tokamak, Phys. Rev. Lett. 107 (2011) 125001
- [8] Tynan G. R. *et al* Recent progress towards a physics-based understanding of the H-mode transition, Plasma Phys. Control. Fusion. 58 (2016) 044003
- [9] Wang H. Q. *et al* New Edge Coherent Mode Providing Continuous Transport in Long-Pulse H-mode Plasmas, Phys. Rev. Lett. 112 (2014) 185004
- [10] McKee G. R. *et al* Increase of turbulence and transport with resonant magnetic perturbations in ELM-suppressed plasmas on DIII-D, Nucl. Fusion 53 (2013) 113011
- [11] Liu S. C. *et al* Edge turbulence characteristics and transport during the ELM mitigation with n=1 resonant magnetic perturbation on EAST, Nucl. Fusion 60 (2020) 082001
- [12] Pecseli H. L. *et al* DRIFT WAVE TURBULENCE IN LOW-BETA PLASMAS, Plasma Phys. Control. Fusion. 25 (1983) 1173
- [13] Evensen H. *et al* Optical Fluctuation Measurements of Turbulence Using a Diagnostic Beam on Phaedrus-T, Rev. Sci. Instrum. 63 (1992) 4928
- [14] Chatterjee R. *et al* First results from the phase contrast imaging system on TEXT-U, Rev. Sci. Instrum. 68 (1997) 676 [15] Peebles W. A. *et al* Fluctuation Measurements in the Diii-D and Text Tokamaks Via Collective Scattering and Reflectometry, Rev. Sci. Instrum. 61 (1990) 3509

- [16] Deng B. H. *et al* Electron cyclotron emission imaging diagnostic of T-e profiles and fluctuations, Phys. Plasmas 8 (2001) 2163
- [17] Maqueda R. J. *et al* Gas puff imaging of edge turbulence (invited), Rev. Sci. Instrum. 74 (2003) 2020
- [18] Zweben S. J. *et al* Invited Review Article: Gas puff imaging diagnostics of edge plasma turbulence in magnetic fusion devices, Rev. Sci. Instrum. 88 (2017) 041101
- [19] Stotler D. P. *et al* Three-dimensional neutral transport simulations of gas puff imaging experiments, Contrib. Plasm. Phys. 44 (2004) 294
- [20] Stotler D. P. *et al* Atomic physics in ITER The foundation for the next step to fusion power, Atomic and Molecular Data and Their Applications 901 (2007) 95
- [21] Burgos J. M. M. *et al* Time-dependent analysis of visible helium line-ratios for electron temperature and density diagnostic using synthetic simulations on NSTX-U, Rev. Sci. Instrum. 87 (2016) 11E502
- [22] Goto M. Collisional-radiative model for neutral helium in plasma revisited, J Quant Spectrosc Ra 76 (2003) 331
- [23] Fujimoto T. Collisional-Radiative Model for Helium and Its Application to a Discharge Plasma, J Quant Spectrosc Ra 21 (1979) 439
- [24] Maqueda R. J. *et al* Edge turbulence measurements in NSTX by gas puff imaging, Rev. Sci. Instrum. 72 (2001) 931 [25] Zweben S. J. *et al* Edge turbulence imaging in the Alcator C-Mod tokamak, Phys. Plasmas 9 (2002) 1981
- [26] Fuchert G. *et al* Blob properties in L- and H-mode from gas-puff imaging in ASDEX upgrade, Plasma Phys. Control. Fusion. 56 (2014) 125001
- [27] Shesterikov I. *et al* Development of the gas-puff imaging diagnostic in the TEXTOR tokamak, Rev. Sci. Instrum. 84 (2013) 053501
- [28] Nishino N. *et al* Edge turbulence measurement in Heliotron J using a combination of hybrid probe system and fast cameras, J. Nucl. Mater. 438 (2013) S540
- [29] Yuan B. et al Development of a new gas puff imaging diagnostic on the HL-2A tokamak, J Instrum 13 (2018) C03033
- [30] Liu S. C. *et al* New dual gas puff imaging system with up-down symmetry on experimental advanced superconducting tokamak, Rev. Sci. Instrum. 83 (2012) 123506
- [31] Wan B. N. *et al* Recent advances in EAST physics experiments in support of steady-state operation for ITER and CFETR, Nucl. Fusion 59 (2019) 112003
- [32] Shannon C. E. Communication in the Presence of Noise, P Ire 37 (1949) 10
- [33] Xu G. S. *et al* Study of the L-I-H transition with a new dual gas puff imaging system in the EAST superconducting tokamak, Nucl. Fusion 54 (2014) 013007
- [34] Shao L. M. *et al* Velocimetry of edge turbulence during the dithering L-H transition with dynamic programming based time-delay estimation technique in the EAST superconducting tokamak, Plasma Phys. Control. Fusion. 55 (2013) 105006
- [35] Xu G. S. *et al* A Dip Structure in the Intrinsic Toroidal Rotation Near the Edge of the Ohmic Plasmas in EAST, Plasma Sci. Technol. 13 (2011) 397